http://dx.doi.org/10.5935/0103-5053.20150225

J. Braz. Chem. Soc., Vol. 26, No. 12, 2545-2557, 2015.
Printed in Brazil - ©2015 Sociedade Brasileira de Química
0103 - 5053 $6.00+0.00

Article

NIR Luminescence from Sol-Gel Er^{3+} Doped SiO_2:GeO_2 Transparent Gels, Nanostructured Powders and Thin Films for Photonic Applications

Lauro J. Q. Maia,*[a] Rogéria R. Gonçalves,[b] Anderson S. L. Gomes[c] and Sidney J. L. Ribeiro[d]

[a]*Instituto de Física, UFG, Campus Samambaia, CP 131, 74001-970 Goiânia-GO, Brazil*

[b]*Departamento de Química, Faculdade de Filosofia, Ciências e Letras de Ribeirão Preto, USP, Av. Bandeirantes, 3900, 14040-901 Ribeirão Preto-SP, Brazil*

[c]*Departamento de Física, UFPE, Cidade Universitária, 50670-901 Recife-PE, Brazil*

[d]*Departamento de Química Geral e Inorgânica, Instituto de Química, UNESP, CP 355, 14801-970 Araraquara-SP, Brazil*

Samples of $(1 - x)SiO_2$:$xGeO_2$ compositions, containing x = 10 and 20, and doped with Er^{3+}, were prepared by a simple sol-gel route. Homogeneous and transparent gels were synthesized and xerogels were obtained by gel annealing from 700 ºC to 1100 ºC. Films exhibiting high transmittance in the visible and near infrared were deposited by spin-coating technique using the colloidal precursors. The materials were characterized structurally and microstructurally by some techniques. Spherical completely amorphous and tetragonal GeO_2 nanocrystals from 3.7 nm to 25.0 nm in diameter embedded in silica-rich amorphous phase materials were obtained. The optical properties were studied by transmission spectra from ultraviolet to near infrared region, photoluminescence measurements in the infrared region, and the average lifetime of the metastable state $^4I_{13/2}$ of Er^{3+} ions were determined. The 1 mol% Er^{3+} doped host with x = 20 have an infrared emission 4.9 times higher than the compound containing x = 10, and the Er^{3+} $^4I_{13/2}$ level present lifetime between 15.0 ms and 7.5 ms. The optical band gap and refractive index values were determined, as well as the Sellmeier parameters. Finally, rib channel waveguides using femtosecond laser etching technique on silica substrates were obtained with width of 15 mm. The 1 mol% Er^{3+} doped $80SiO_2$:$20GeO_2$ compounds can be applicable in integrated optical systems.

Keywords: Er-doped SiO_2:GeO_2, simple sol-gel route, nanocomposite, optical and structural properties, optical waveguide

Introduction

Growing demand of optical systems and their future potentialities stimulate research for photonic devices development, which are characterized by a network system with excellent flexibility and larger information capacities at much faster rates. Among several devices in telecommunication systems, the invention of optical amplifiers can be compared to that of the transistors in electronics in terms of its technological impact.[1] The technology to directly amplify the light signal without the conversion of light/electricity/light has been achieved with rare earth doped fibers which realize ideal amplification with high gain and low noise.[2] Optical properties of rare-earth ions incorporated in glass hosts are of great interest in opto-electronic technology.[3] Rare earth trivalent ions in some solid compounds emit light at characteristic wavelengths due to intra-4f or internal 4f-5d transitions. In the case of Er^{3+}, the emission at 1540 nm corresponds to a dipole forbidden intra 4f transition from $^4I_{13/2}$ to $^4I_{15/2}$, coinciding with the low-loss window of standard optical telecommunication silica fiber, allowing its use in optical amplifiers for C telecommunication band.

Recently, remarkable progress has been achieved in the development of single-mode Er-doped optical fiber amplifiers and lasers.[4-6] Development of Er-doped planar waveguide amplifiers has also been investigated to be applied in integrated optical systems, but integrated optical amplifiers should be as small as possible (a few centimeters),[7,8] so that much higher rare-earth concentrations

*e-mail: lauro@ufg.br

are required than in Er-doped fiber amplifiers (EDFAs). However, due to the onset of concentration quenching at low doping levels in silica hosts, the relatively low gains/unit length which can be achieved has made such development difficult. Consequently, SiO_2 is an unsuitable host in small, compact amplifiers due to the low erbium solubility.

However, there is a great interest to insert other elements into the SiO_2 host, for example GeO_2, resulting in $(1 - x)SiO_2$:$xGeO_2$ binary system, which is promising for integrated optics due to low propagation losses in the visible and infrared regions and their photosensitivity that allow the channel waveguides and Bragg mirrors photo-inscription using ultraviolet light.[9,10]

Furthermore, there is a motivating aspect for the use of homogeneous glassy or nanostructured thin films as waveguides because there are no grain boundaries, which can cause a high optical loss as in polycrystalline films. Recent results presented on the literature confirm that ceramic laser materials became an attractive alternative to single crystal due to their easy manufacture and low cost.[11] In this way, the nanostructured Er^{3+} doped SiO_2:GeO_2 host are interesting materials for integrated amplifiers and laser medium.

The sol-gel process allows the preparation of bulk materials, thin films as well as powders, which can be used to prepare glasses, glass-ceramics and ceramics. The major advantages of this low temperature chemical route are the large variety of materials exhibiting not only a multicomponent host but also can be doped to modify their properties, the excellent control of the chemical purity, low cost of fabrication and possibility to obtain nanostructured powders with a controlled size particle for transparent ceramics manufacture. Since thin sol-gel films can be easily made through dip-coating or spin-coating techniques, this method is considered ideal for the fabrication of active integrated optical devices like optical waveguide lasers and amplifiers.[12-15]

The sol-gel process has been used for the preparation of SiO_2:GeO_2 compounds.[16-20] Jing *et al.*[16] studied thick films of $30SiO_2$:$70GeO_2$ obtained from tetraethylorthogermanate ($Ge(OC_2H_5)_4$, TEOG) and diethylorthosilicate (DEOS). Jang *et al.*[18] have used TEOG and tetraethylorthosilicate ($Si(OC_2H_5)_4$, TEOS) to obtain thin films by spin-coating technique. Ge-doped SiO_2 glasses was synthesized by sol-gel process using TEOS and 3-trichologermanium propanoic acid ($Cl_3GeCH_2CH_2COOH$) as starting materials.[19] Acid-catalyzed solutions of γ-glycidoxypropyl-trimethoxysilane mixed with germanium isopropoxide are used as matrix precursors to prepare Nd^{3+} doped SiO_2:GeO_2 thin films by spin-coating technique.[20] Also, glasses of $90SiO_2$:$10GeO_2$ composition, in mol%, have been prepared by the sol-gel method in which TEOS and TEOG were used as starting materials.[17] In all these procedures, the authors have used germanium alkoxides, which are very reactive with water molecules, promoting very fast hydrolysis and condensation reactions, and consequently, an atmosphere control is required for obtaining a transparent, homogeneous and nanostructured material.

Recently, Sigoli *et al.*[21] have published results on the Er^{3+} and Yb^{3+} co-doped SiO_2:GeO_2 planar waveguide onto silica on silicon substrates obtained by the sol-gel process combined with a spin-coating technique. The compositions of studied samples were $95.8SiO_2$:$4.2GeO_2$ doped with 0.1-2.0 mol% of Er^{3+} and 0.7-1.4 mol% of Yb^{3+}, which is based in a low Ge content host. For the sample preparation, firstly silica nanoparticles were prepared by hydrolysis of tetraethyl orthosilicate (TEOS) in basic media, and the germanium precursor solution was obtained by adding GeO_2 into ethylene glycol with NH_4OH. The SiO_2-GeO_2 precursors mixture were doped with different amounts of Er and Yb chloride salts, followed by addition of 30 wt.% aqueous solution of polyvinyl alcohol (PVA), resulting in a transparent sol. The films were prepared using a multilayer process, followed by a posterior heat treatment at 1150 °C for 60 s using a rapid thermal annealing (RTA) furnace. As a conclusion, the authors claimed that the rapid thermal annealing under nitrogen flows avoided the crystallization of the films and the rare-earth cluster formation, being effective for material densification, however the effect of the Ge content on the Er^{3+} emission was not evaluated.

In this paper, we present the development of a simple and relatively low cost sol-gel route for obtaining homogeneous Er^{3+} doped $(1 - x)SiO_2$:$xGeO_2$ with x = 10 and 20 nanometer-sized powders and transparent thin films, which are cracks and porous free with relatively thick layers. We describe and discuss the thermal, structural, micro-structural, optical transmission properties and their correlation and influence on the near infrared (NIR) emission of Er^{3+} ions from the samples. Besides, the paper reports on the preparation of planar and channel waveguides based on Er^{3+} doped $80SiO_2$:$20GeO_2$. This work contributes to establish a new sol-gel route, without requirement of a specific atmosphere control, which can be used to prepare materials containing germanium.

Experimental

Sample preparation

Crystalline GeO_2 has mainly two crystalline structures: one is hexagonal and the other is tetragonal. Hexagonal

GeO_2 is somewhat soluble in water (0.453 g *per* 100 g of water, 25 °C), while tetragonal GeO_2 is insoluble.[22] On the other hand, GeO_2 is soluble in H_2SO_4/NH_4OH basic solutions at pH around 9-10,[22] but insoluble in acid solutions.[23] Based on these information, initially we tested several possibilities to mix TEOS in the germanium oxide (GeO_2) previously dissolved in a solution of pH ca. 10, but a fast precipitation takes place in all tests. Another chemical route was dissolve GeO_2 in an aqueous solution containing ethylenediamine in which could be obtained a transparent and stable sol, but a fast precipitation takes place when TEOS is included. Finally, we could prepare a stable sol with tetramethylammonium hydroxide (TMAH) solution (aqueous solution containing 25% in mass of TMAH). The TMAH solution is very efficient to dissolve GeO_2, and it allowed include TEOS, as will show below.

Sols preparation

The starting solutions was prepared using the tetraethylorthosilicate (TEOS, $Si(OC_2H_5)_4$, Alfa Aesar, 99% purity), germanium oxide (GeO_2, Sigma-Aldrich, 99.999% purity), erbium chloride ($ErCl_3$, Reacton, 99.9% purity), tetrametylammonium hydroxide solution (TMAH, $(CH_3)NOH$, Sigma-Aldrich, solution of 25 wt.% in water), isopropanol (iPrOH, Chemis, P.A.), and *D*-sorbitol (Sigma-Aldrich, 99% purity).

Firstly, the TEOS was pre-hydrolysed ($1Si(OC_2H_5)_4:2H_2O$, molar ratio) during 1 h, for x = 10 and x = 20 was used 3.838 mL and 1.706 mL of TEOS, respectively (named Sol1). 200 mg of GeO_2 was diluted in 2 mL of TMAH solution, 2 mL of iPrOH, and 2 mL of deionized H_2O (named Sol2). Considering the addition of rare-earth chlorides (as $ErCl_3$, $YbCl_3$ or $EuCl_3$) in basic medium was necessary include a small amount of *D*-sorbitol to prevent rare earth hydrolysis and precipitation. The $ErCl_3$ was dissolved in *D*-sorbitol and deionized water ($1ErCl_3:5D$-sorbitol:$500H_2O$, molar ratio) named Sol3. A mixture of Sol1, Sol2, and Sol3 were performed under vigorous stirring during 1 h and aged for 24 h. During the aging period occurs the formation of some precipitates. Finally, 1 mL of deionized water was added under vigorous stirring for around 30 min, and we could obtain a transparent and stable sol. All procedure was performed in atmospheric air, and did not require special atmosphere.

Films deposition

The sols were filtered with Millipore 0.2 mm and used for thin films deposition at 25 °C. Before the film depositions, the substrates were cleaned with a detergent (biodegradable anionic surfactant), rinsed with deionized water and placed inside a HNO_3 + HCl solution (16 HNO_3 + 28 HCl + 56 H_2O, molar ratio) during 5 min. The substrates were then rinsed once again in deionized water, ethyl alcohol and dried with anhydrous air.

Thin films were deposited on sodalime glass substrates using the spin-coating technique. Rotation speed and spin time were fixed at 1500 rpm, and 10 s, respectively. Before further coating, each layer was annealed in air for 2 h at 400 °C using a heating rate of 2 °C min^{-1}. The final films were obtained after 3 coatings and heat-treated at 700 °C during 2 h using a heating rate of 5 °C min^{-1} in atmospheric air.

Gels and powders preparation

In parallel, the sol obtained after films preparation was maintained in an oven at 45 °C during 6 days in atmospheric air, to obtain transparent monoliths (transparent dried gels). Next, the samples were heat treated 100 °C for around 24 h, annealed in an electrical furnace at 400 °C for 5 h, and 900 °C for 2 h or 1100 °C for 2 h using a heating rate of 5 °C min^{-1} in atmospheric air, to obtain nanocomposite powders.

Characterization

The dried gels at 45 °C during 6 days, were subjected to thermal analysis using an SDTQ600 TA Instruments Model thermoanalyzer which records differential thermal analysis (DTA) and thermogravimetry (TGA) simultaneously. Samples (25 mg) were put into α-alumina crucibles, using calcined α-alumina as a reference material. The heating rate was 10 °C min^{-1} and the thermal analysis was carried out in flowing synthetic air (50 mL min^{-1}) as the measurements were taken.

The gel and powder samples were mixed with dried KBr and pressed into pellets, and the corresponding Fourier transform infrared (FTIR) spectra were collected in the 4000-400 cm^{-1} range using a FTIR Perkin Elmer 2000 spectrometer with 4 cm^{-1} resolution.

The crystalline phases were analyzed by X-ray diffraction (XRD) technique. XRD measurements were performed at room temperature in a transmission geometry using a Siemens D5000 equipped with a nickel filter using Cu Kα radiation (λ = 1.5406 Å) and a graphite monochromator. XRD scans were collected from 5 to 60° (2θ) using a scan rate of 0.6 degree min^{-1} and an increment of 0.02°.

Images of the powder samples were obtained by high-resolution transmission electron microscopy (HRTEM) using a Philips CM200 microscope.

Optical transmission spectra in the UV-Visible-NIR near regions (200-2000 nm) were recorded at room temperature using a Cary 500 spectrophotometer (600 nm min^{-1}, resolution of 0.5 nm).

The photoluminescence (PL) spectra at room temperature were registered on a spectrofluorometer (SpectraPro 300i, Roper Scientific), equipped with an InGaAs detector (ID-441C) and a double monochromator with resolution of 1.8 nm (Spex 212L). The excitation source was the 488 nm line of an Ar^+ laser (500 mW) (Innova 300C, Coherent Inc.).

The lifetime at room temperature was acquired with a InGaAs detector using the 488 nm line of an Ar^+ laser (500 mW) (Innova 300C, Coherent Inc.), a chopper (SR540, Stanford Research Systems Inc.) operating at 10 Hz, a digital oscilloscope (54600B, Hewlett Packard), and an optical filter RG1000 to eliminate the excitation signal.

Channels were written onto the surface of films deposited on silica substrates using a femtosecond laser etching technique. To this end, an 800 nm Ti-sapphire laser emitting 150 fs, 76 MHz mode-locked pulses was focused on the film surface with an objective lens. The spot size of the focused beam was 5 mm at the focal point, and the average power of the laser was 10 mW. The scanning speed was 0.5 mm s^{-1}. 3D surface image of the channel waveguide was measured on a FORMTRACER profilometer from Taylor Hobson Precision model SV-C525.

Results and Discussion

Thermal properties

Figure 1 presents the TGA and DTA curves of the $90SiO_2$:$10GeO_2$ (x = 10) and $80SiO_2$:$10GeO_2$ (x = 20) gels doped with 1 mol% of Er^{3+}. As can be seen, a mass loss (16.5% for x = 10, and 12.5% for x = 20) was observed between 35 and 160 °C due to desorption of the adsorbed moisture and the evaporation of solvents and dehydration. The samples showed a mass loss of approximately 33.8% for x = 10 and 45.5% for x = 20 between 160 and 330 °C due to an elimination of residual solvents (peak at 210 °C for x = 10 and x = 20) and combustion/oxidation process (exothermic peaks at 264 and 317 °C for x = 10, and at 244, 264 and 297 °C for x = 20). From 330 to 500 °C, exothermic reactions was observed centered at 371 and 423 °C for x = 10, and at 350, 450 and 480 °C for x = 20, with mass loss of 2.1% for both samples, due to final oxidation process. Between 500 and 700 °C, any reactions occurred.

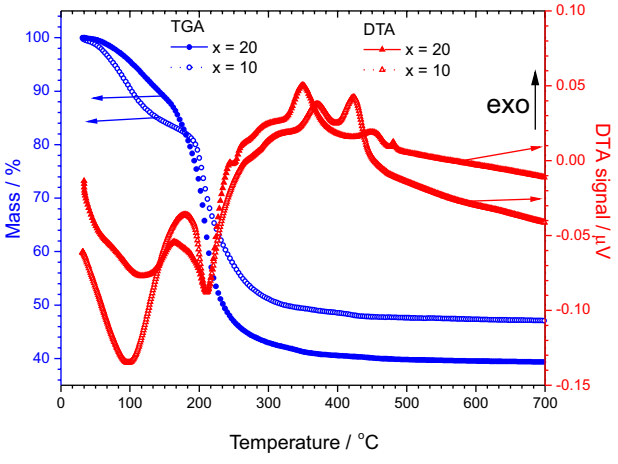

Figure 1. TGA and DTA curves for gels dried at 45 °C during 6 days of (1 – x)SiO_2:xGeO_2 with x = 10 and 20 compositions. Reference and sample crucibles of alumina, air atmosphere and heating rate of 5 °C min^{-1}.

Structural properties

In order to better understand the structural changes from gels (45 °C and 100 °C) and amorphous powders (900 °C) to partially crystallized powders (1100 °C) for x = 10, FTIR spectroscopy was used. IR spectra are reported in Figure 2 between 4000 and 400 cm^{-1}. For x = 20 only

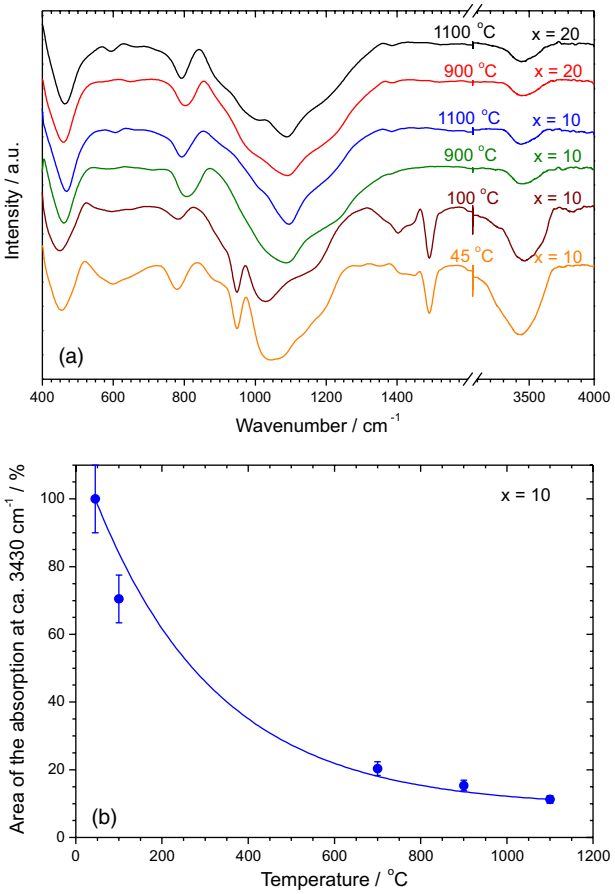

Figure 2. (a) FTIR spectra for gels dried at 45 °C during 6 days and powders of (1 – x)SiO_2:xGeO_2 with x = 10 and 20 compositions heat treated 100, 900 and 1100 °C; (b) area of the absorption at ca. 3430 cm^{-1} as a function of temperature for x = 10.

samples heat-treated at 900 °C and 1100 °C were presented and compared with x = 10 composition.

The bands at 595, 1404 and 1490 cm^{-1} in the spectra of x = 10 at 45 °C and 100 °C are due to absorptions of C–C, C–CH_2, N–O and N–CH_3 groups stretching, and CH and CH_2 groups deformation. These organic compounds were completely eliminated after annealing at 700, 900 and 1100 °C. In the 1400-400 cm^{-1} range, the most intense bands refer to the SiO_2 network vibrational modes. Besides that, vibrational modes related to Si–OH, Si–O–Ge, and Ge–O–Ge vibrational modes also appear in this region. The SiO_2 network can be characterized by three main Si–O–Si vibrational modes, which can be observed in detail in Figure 2, at 460, 800 and 1090 cm^{-1}. The peak at 460 cm^{-1} is attributed to transverse-optical (TO) rocking motions perpendicular to the Si–O–Si plane of the oxygen bridging two adjacent Si atoms. The second one located at 800 cm^{-1} is due to the TO symmetric stretching of the O atom along a line bisecting the Si–O–Si angle. The broad band at 1090 cm^{-1} corresponds to the back and forth motion of the oxygen atom along a line parallel to the Si–Si axis, which results in a TO antisymmetric stretching. The latter band is accompanied by a shoulder at 1250 cm^{-1}, characteristic of an admixture of TO and LO (longitudinal optical) components, which is more intense in porous materials.[24,25] In the case of the samples annealed at low temperature, the bands around 1030 and 1200 cm^{-1} show a shift and broadening in comparison with the samples annealed at higher temperature, corroborating with the presence of organic groups and an incomplete hydrolysis and condensation process, originating a porous material.

Concerning the presence of germanium oxide, in the literature is well reported that the infrared absorption band of GeO_2 show a broad band centered at 900 cm^{-1}, attributed to Ge–O vibrations in GeO_4 tetrahedral in which every oxygen atom is bonded to another germanium atom.[26] In Figure 2, a shoulder at 1000 cm^{-1} and 900 cm^{-1} appears increasing in intensity with the germanium content, and can be attributed to the Ge–O–Ge and Si–O–Ge vibrational modes. The presence of GeO_2 can be also attested analyzing the spectra region between 500-650 cm^{-1}. Vibrational modes attributed to the Ge–O links in this region are also reported in the literature, and can be seen in the samples annealed at higher temperatures.

Bands at 1670 cm^{-1} and 3440 cm^{-1} are also observed due to vibrational modes of the water molecules or hydroxyl groups that aware reduced gradually by increasing the annealing temperature, as previously observed in the TGA results and discussions. For the samples heat treated at 45 and 100 °C, a vibrational mode attributed to the Si–OH groups (silanols) appears at around 950 cm^{-1}, which disappear at higher temperatures.[24,25]

Similar FTIR spectra of compounds with x = 10 and x = 20 annealed at 900 °C were observed, suggesting the presence of structure similarity. However, increasing the temperature to 1100 °C, peaks at 592 and 665 cm^{-1} for x = 10 and 20 appears, which can be attributed to GeO_2 particle formation in silica host. On the other hand, the band at 808 cm^{-1} for 900 °C shifts to 792 cm^{-1} for 1100 °C (x = 10) and from 802 cm^{-1} for 900 °C to 792 cm^{-1} for 1100 °C (x = 20), which indicates some contribution of Ge–O to the band around 800 cm^{-1}.

In Figure 3 are shown the XRD patterns for x = 10 and 20 doped with 1 mol% of Er^{3+} heat treated at 700, 900 and 1100 °C, where the peaks are indentified and compared with those reported in the literature. A structural change clearly occurs as a function of the heat treatment temperature, which denotes a direct dependence of the crystalline phase contents. A large background between 15° and 35° in 2θ was detected in all diffractograms, which corresponds to the amorphous silica-based host, as also observed by Ferrari *et al.*[27] for SiO_2-Ta_2O_5 compounds. In accordance with JCPDS card number 73-1306, the peaks at 22.5; 31.5; 36.1; 48.7; and 57.1 degree are due to (101); (102); (112) and (200); (212); (213) and (301) planes of GeO_2 nanocrystals with tetragonal structure (space group $P4_12_12$ (92)) and the cell parameters are a = 4.99 Å, and c = 7.06 Å (C = 1.4148 and Z = 4). From the XRD results, the GeO_2 crystals into the silicate host appear only after heat treatment at 1100 °C.

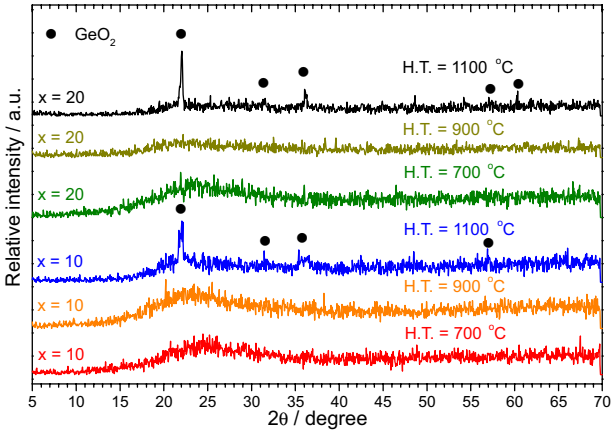

Figure 3. X-ray diffraction patterns for powders of (1 – x)SiO_2:xGeO_2 with x = 10 and 20 heat treated at 700, 900 and 1100 °C.

Morphological properties

Figures 4a and 4d show TEM images of the compounds annealed at 900 °C for 2 h containing x = 10, in which spherical GeO_2 nanoparticles of 3.7 ± 0.1 nm in diameter is dispersed into the silicate host (which were not detected by XRD results). For the compounds with x = 20 annealed

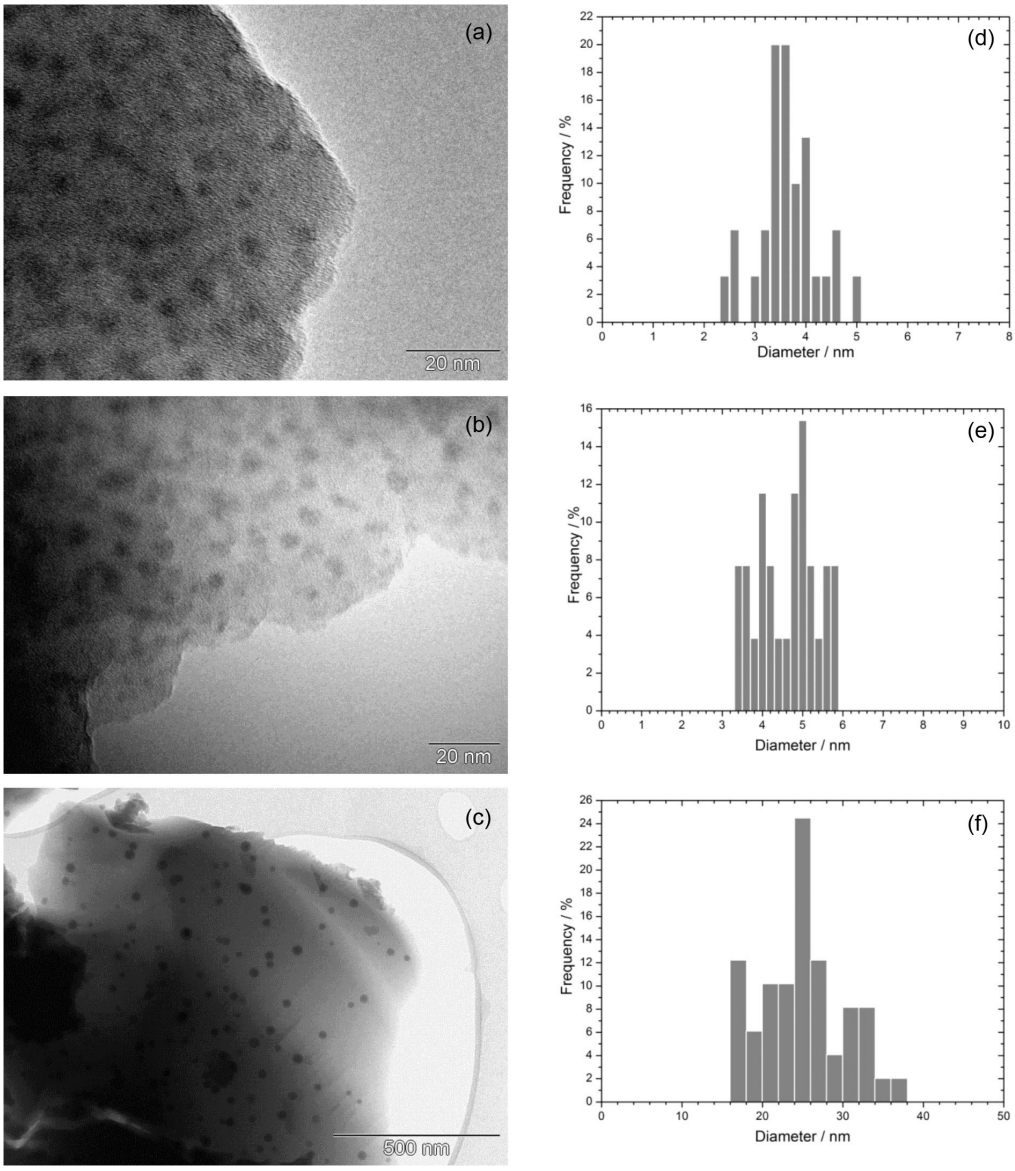

Figure 4. TEM images and GeO_2 nanoparticles size distribution of powders from (1 – x)SiO_2:xGeO_2 compositions, with: (a) x = 10 and heat-treated at 900 °C; (b) x = 20 and heat-treated at 900 °C; (c) x = 20 and heat-treated at 1100 °C; (d) x = 10 and heat-treated at 900 °C; (e) x = 20 and heat-treated at 900 °C; (f) x = 20 and heat-treated at 1100 °C.

at 900 °C, Figures 4b and 4e, spherical GeO_2 nanoparticles of around 4.6 ± 0.2 nm in diameter can be observed, and for x = 20 heat-treated at 1100 °C the diameter size increase to 25.0 ± 0.8 nm (Figures 4c and 4f). In fact, the diameter size of GeO_2 nanocrystals is almost the same as the content of the germanium oxide increases, at least for concentration of 10 and 20 mol%. Due to low crystallinity and the small size of the GeO_2 nanoparticles, they were not detected by XRD patterns (Figure 3) after annealing at 900 °C. Increasing the annealing to 1100 °C for x = 20, GeO_2 nanoparticles with higher diameter were crystallized and consequently could be detected by XRD patterns (Figure 3).

All the samples show GeO_2 nanoparticles with diameter lower than λ/20, considering as λ the wavelength of the Er^{3+} pumping (λ = 980 nm, λ/20 = 49 nm) and emission (λ = 1540 nm; λ/20 = 77 nm) used in telecommunication systems as optical amplifiers. Therefore, the presence of GeO_2 nanoparticles will not reduce significantly the NIR propagation signal, i.e., the contribution to the losses due to volume scattering is not significant considering these compositions in waveguides for infrared light.[28,29] Besides, films heat-treated around 700 °C could be even better for waveguide application, since at these temperatures any GeO_2 nanoparticles are distributed in the silicate host.

To evaluate the dispersion behavior of Er^{3+} ions in x = 20 compounds heat-treated at 900 °C and 1100 °C, were used the energy dispersive X-ray (EDX) to collect spectra on the silica-rich matrix and on the GeO_2 nanoparticles, as

can see in Figure 5. For 900 °C, note that a higher erbium peak intensity in GeO_2 nanoparticles in comparison to that in silicate matrix region. However, for 1100 °C in which nanoparticles have diameter of around 25.0 ± 0.8 nm, a much higher concentration of Er^{3+} ions around/into the GeO_2 nanoparticles than in silica-rich matrix is observed, indicating that Er^{3+} solubility in GeO_2 nanoparticles are higher than in silicate host, especially at higher temperatures.

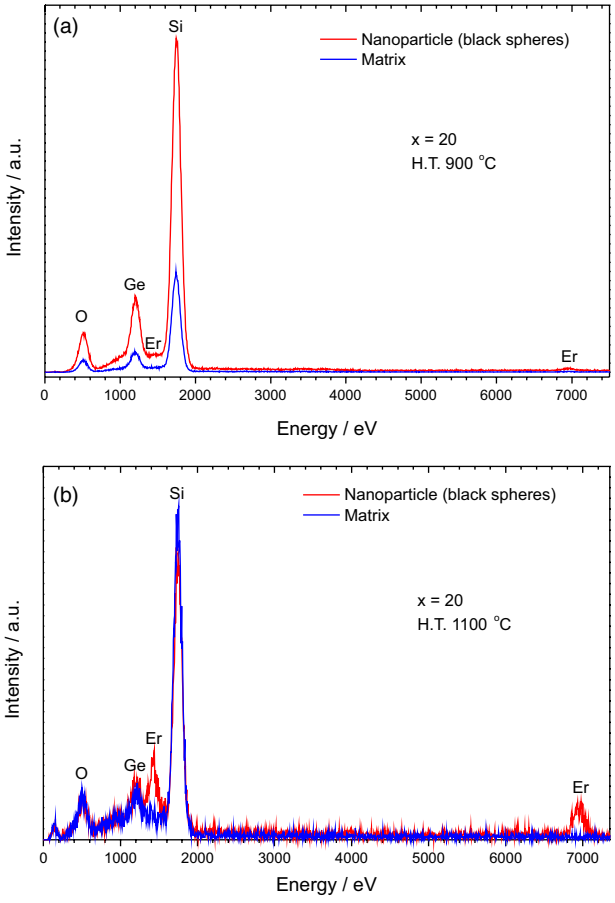

Figure 5. EDX spectra of x = 20 doped with 1 mol% of Er^{3+} heat-treated at 900 °C and 1100 °C. The thin lines are EDX spectra in a light gray region (matrix) and the thick lines are EDX spectra in a dark gray region (nanoparticles = black spheres) measured by TEM (Figures 4b and 4c, respectively).

The chemical procedure developed here allows obtaining stable and uniform –Si–O–Ge–O–Si– network in sols, gels and films as well as powders synthesized at relative low temperatures. With heat-treatment phase separation was observed. It is well known that different ions segregate in silica network, as shown for SiO_2-ZrO_2,[28,30] SiO_2-TiO_2,[31] and SiO_2-Ta_2O_5[27,29] leading to nanocrystals. The same effect occurs for SiO_2-GeO_2 system studied here. Increasing the energy (heat-treatment temperature) and the Ge content into the matrix, more ions quantity are expelled from SiO_2 network progressively and due to this the GeO_2 particles into silica matrix increase in size significantly only at 1100 °C. On the other hand, the literature have mentioned that rare-earth solubility in silica is < 10^{18} ions cm^{-3},[32] and we have shown in this work that larger amounts of Er^{3+} are located around/into GeO_2 particles by EDX results, confirming the Er^{3+} migration in samples heat treated at high temperatures.

Optical properties

Gels

An illustrative image of the obtained gel is included in the Figure 6 took by a digital camera. Also, in Figure 6 we present a UV-Vis-NIR spectrum of the $90SiO_2$:$10GeO_2$ gel doped with 1 mol% of Er^{3+}. Similar results were obtained for different concentrations of Er^{3+} and for x = 20 (not shown here). The gels were well transparent with high mechanical resistance allowing be handled. The f-f transitions of the Er^{3+} ions were detected at 269, 322, 366, 378, 406, 452, 489, 521, 547, 653, 886, 981 and 1490 nm from $^4I_{15/2}$ level to $^4G_{9/2}$, $^2P_{3/2}$, $^2G_{9/2}$, $^4G_{11/2}$, $^2H_{9/2}$, $^4F_{3/2}$, $^4F_{7/2}$, $^2H_{11/2}$, $^4S_{3/2}$, $^4F_{9/2}$, $^4I_{9/2}$, $^4I_{11/2}$ and $^4I_{13/2}$ level, respectively. The bands centered at 1161, 1226, 1339, 1350, 1363, 1600, 1664, 1703, 1720, 1745, 1782, 1812, 1857, and 1937 nm are due to organic compounds (CH_3, CH_2, C–H, C–C, C=C, C–O, C=O, C–N, C=N, O–H, N–H, N-O, and/or N=O, etc.) into the gel from precursor compounds.

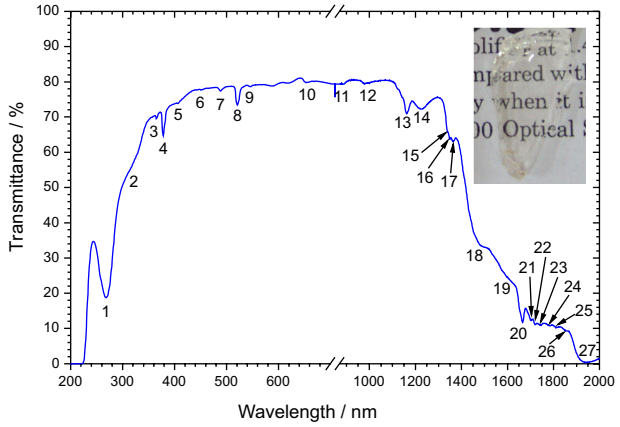

Figure 6. Transmission spectrum in the UV-Vis-NIR regions for gels with x = 10 doped with 1 mol% of Er^{3+} and dried at 45 °C during 6 days.

Powders

Photoluminescence emission spectra in the near infrared region under excitation at 488 nm from the different powders changing composition and doping levels were obtained. In Figure 7a is illustrated the PL emission due to $^4I_{13/2} \rightarrow {}^4I_{15/2}$ transition of Er^{3+} ions in the $90SiO_2$:$10GeO_2$ powders heat-treated at 900 °C for different Er^{3+} concentrations, in the

inset were included the integrated band intensity of these spectra as a function of Er^{3+} concentration. Note that the PL emission increase from 0.05 to 0.5 mol% Er^{3+}, and higher concentrations the PL emission decrease gradually, showing that for x = 10 and annealing at 900 °C the best rare-earth doping is around 0.5 mol%, being for this matrix the solubility limit. Increasing the heat treatment to 1100 °C (Figure 7b), the PL emission maximum is observed for 0.8 mol% (almost the same intensity of 0.5 mol% sample) but the emission intensities are lower than that observed for 900 °C.

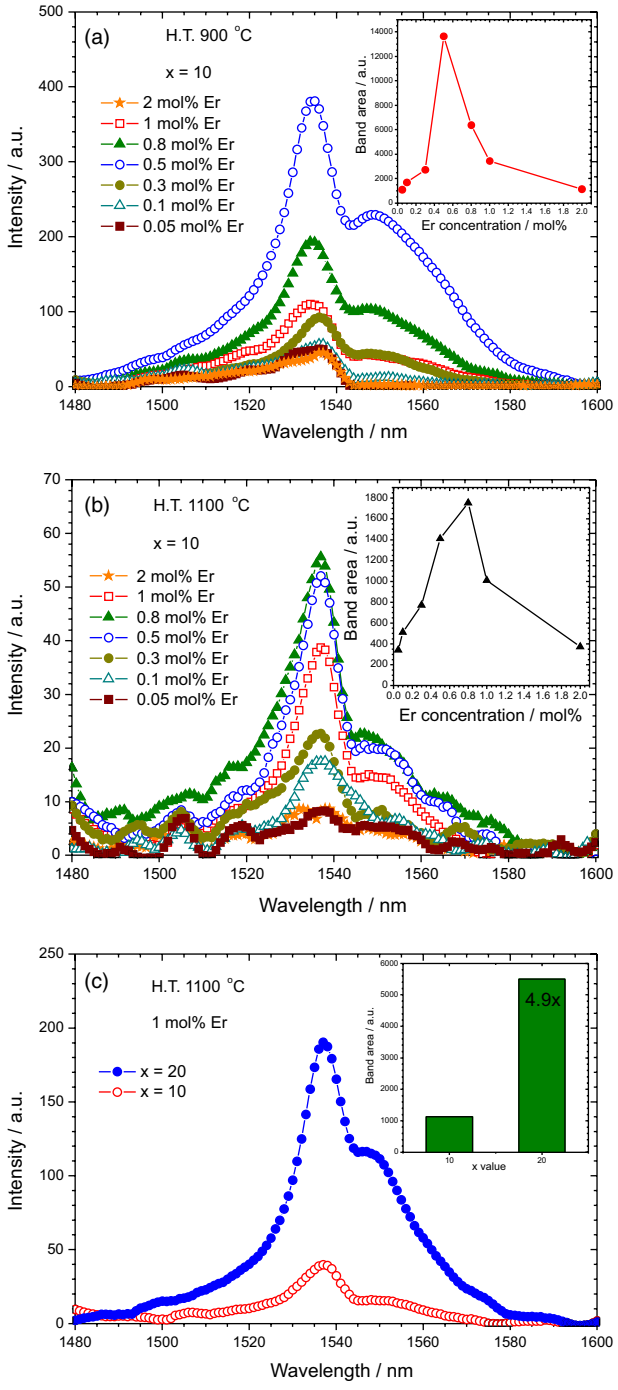

Figure 7. PL emission spectra under 488 nm excitation for powders doped with different erbium concentrations of: (a) x = 10 composition, and heat-treated at 900 °C; (b) x = 10 composition, and heat-treated at 1100 °C; (c) x = 10 and 20, doped with 1 mol% of Er^{3+}, and heat-treated at 1100 °C.

This is an indication that the Er^{3+} ions have higher solubility around/into GeO_2 in comparison with silicate host. This is supported by EDX results (Figure 5) that show high concentrations of Er^{3+} ions around/into GeO_2 nanoparticles at 1100 °C. However, increasing the temperature, it can favor Er–O–Er clusters formation, which increases energy migration. Besides, the crystallization process, in which Ge–O–Ge, Si–O–Ge and Si–O–Si links breakdown, leads to the formation of defects and non-binding oxygens that favor Er^{3+} ions non-radiative de-excitation and reduce its infrared emission. Probably the energy migration (due to Er–O–Er cluster formation) combined with presence of defects are the main contributions to the observed decrease in intensity for the samples containing higher than 0.8 or 0.5 mol% Er^{3+}.

Note that, the annealing temperature is fundamental to activate Er^{3+} ions in the $90SiO_2$:$10GeO_2$ host, in fact the 900 °C is the most appropriate temperature, when compared to 1100 °C, being limited to 0.5 mol% of Er^{3+} and presenting 30 nm of FWHM (full width at half medium). This concentration limit value is higher than of Er^{3+} doped silica, aluminates and phosphates materials.[33-35] The SiO_2:GeO_2 compositions have potential use as optical amplifiers in integrated systems. In addition, their refractive index are slightly higher than that of silica allowing low losses in silica optical fibers coupling, and the presence of germanium enable diffraction gratings recording using UV lasers by photo-contraction phenomenon.[9,10]

At 1100 °C the FWHM of the emission centered at 1535 nm is around 13 nm, which are smaller than those observed for 900 °C, due to the presence of Er^{3+} ions around/into GeO_2 nanoparticles with higher size and crystallinity (Figures 3 and 4).

Besides, when the GeO_2 concentration is increased to x = 20 ($80SiO_2$:$20GeO_2$) and doped with 1 mol% is observed an emission 4.9 times superior than for x = 10, as presented in Figure 7c. Also, the NIR emission spectra were collected for both samples x = 10 and 20 containing 1 mol% of Er^{3+} and heat-treated at 1100 °C under excitation at 980 nm light from a diode laser (spectra were not shown here), in which was observed the same emission intensity relation among both samples and same spectral shape in comparison to those spectra collected under 488 nm excitation. In previous EDX results, it was observed a higher erbium concentration around/into GeO_2 nanoparticles, leading us to think that GeO_2 crystalline nanoparticles possess higher erbium solubility in comparison to silicate host, preventing clustering

and formation of Er–O–Er links (at least for the samples containing Er^{3+} concentration lower than 0.5 mol%).

Since the luminescence intensity for the both samples (x = 10 and x = 20) annealed at 900 °C doped with 1 mol% of Er^{3+} are similar in NIR region, it was presented in Figure 7 only emission spectra concerning the x = 10 samples. However, when the samples are annealed at 1100 °C the x = 20 sample have higher emission intensity in comparison with that containing x = 10. This can be explained by the hydroxyl groups reduction and relevant portion of Er^{3+} ions migration to nanocrystals (as shown by EDX results). Moreover, GeO_2 compounds have lower phonon energy (740 cm^{-1})[36] than SiO_2 compounds (1075 cm^{-1})[27] favoring an improvement of the Er^{3+} NIR emission. The EDX technique has no high precision to determine the exact Er^{3+} position, i.e., it is not known exactly if they are in higher quantity into or around GeO_2 particles. Also, in samples with x = 20 heat-treated at high temperatures (1100 °C) occurs the formation of higher crystalline GeO_2 particles size than for x = 10, which gives a different light scattering (in excitation and emission), but a higher Er^{3+} solubility associated to low phonon energy can compensate some intensity decrease due to scattering.

Likewise, to study the heat treatment effect and GeO_2 content, the PL decay curves were measured at 1535 nm from $^4I_{3/2}$ level of Er^{3+}, the medium lifetime values were listed in Table 1. In x = 10 with 1 mol% of Er^{3+} occurs the lifetime changes from 15.0 ± 0.5 ms for 900 °C to 7.5 ± 0.5 ms 1100 °C, but when GeO_2 is increased (x = 20) the lifetime is about 12.8 ± 0.5 ms for 1100 °C, corroborating with our previous results and discussions, i.e., low GeO_2 concentration associate to high temperature promote some Er–O–Er clustering or defects generation that reduce active Er^{3+} ions, and high temperatures with higher GeO_2 concentration increase active Er^{3+} ions. In fact, the Er^{3+} infrared PL emissions, lifetime values and structural properties of the host are strongly correlated.

Table 1. Lifetime value for $^4I_{13/2}$ level of Er^{3+} ions in the compositions with x = 10 and 20, and heat-treated at 900 or 1100 °C

Sample	Er^{3+} doping / mol%	Heat treatment / °C	Er^{3+} $^4I_{13/2}$ lifetime / ms
x = 10	1.0	900	15.0 ± 0.5
x = 10	1.0	1100	7.5 ± 0.5
x = 20	1.0	1100	12.8 ± 0.5

The lifetime value for $^4I_{13/2}$ level of Er^{3+} ions in the x = 20 composition heat-treated at 1100 °C is comparable to those values measured by Sigoli *et al.*[21] for $95.8SiO_2$:$4.2GeO_2$ host, which changed between 13.2 and 11.3 ms depending on the Er^{3+} and Yb^{3+} contents.

Thin films

Optical transmission spectra of the $80SiO_2$:$20GeO_2$ films doped with 1 mol% of Er^{3+} were measured continuously from 200 nm to 2000 nm with an UV-Vis-NIR spectrophotometer. Figure 8a displays the transmission spectra of film with 3 layers heat-treated at 700 °C. A high transparency in the visible and infrared regions was detected, higher than 92% at 632.8 nm (the He-Ne laser wavelength used as reference). Other optical property, such as the band gap, was obtained indirectly. Considering the high absorption region, the transmittance (T) followed a simple correlation with absorption coefficient,[37] equation 1, where C is approximately equal to the unity at the absorption edge and d is the thickness of the thin films. The relation between the absorption coefficient α and incident photon energy hν for allowed direct transition can be written as equation 2,[37] where A is constant and E_g is the direct band gap.

$$T = Ce^{-\alpha d} \quad (1)$$

$$(\alpha h\nu)^2 = A(h\nu - E_g) \quad (2)$$

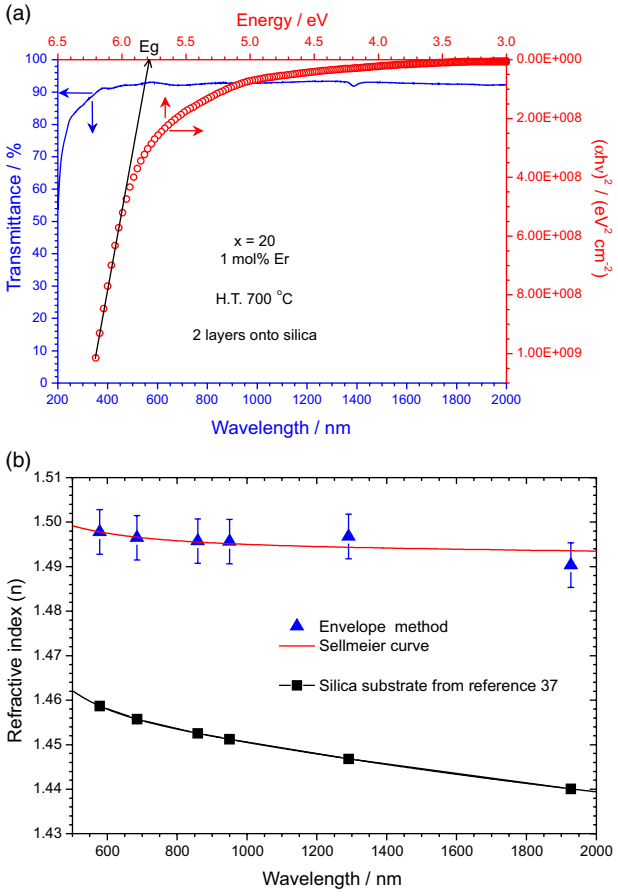

Figure 8. (a) Transmission spectra in the UV-Vis-NIR region for film with x = 20 doped with 1 mol% of Er^{3+}, deposited by spin-coating onto silica substrate (3 layers), and heat-treated at 700 °C; (b) refractive index values dispersion and Sellmeier curve for x = 20 and values for silica substrate.

The $(ah\nu)^2$ *versus* $h\nu$ plot for the thin film is shown in Figure 8a. A linear behavior can be observed in a certain range of the curves, supporting the interpretation of direct E_g band gap for thin film.[37] Therefore, the E_g band gap can be obtained by extrapolating relation (2) around 5.79 eV (214 nm). This value is comparable with those reported by Jing *et al.*[16] of 5.5 eV (225 nm) for $30SiO_2$:$70GeO_2$ thick films. On the other hand, works on glasses with $90SiO_2$:$10GeO_2$ composition developed by Nishii *et al.*[38] and Shigemura *et al.*[17] obtained an optical band gap of ca. 7.1 eV (175 nm), and ca. 6.0 eV (207 nm), respectively. All these values is influenced by the GeO_2 nanosized into the matrix and an absorption band at ca. 5 eV (248 nm) assigned to different kinds of intrinsic germanium-related oxygen-deficient centers in glasses, which consist of neutral oxygen monovacancy [(NOMV)≡Ge–Ge≡ or ≡Ge–Si≡] and neutral oxygen divacancy [(NODV)-Ge^{2+}].[16,17,39] In our optical transmission spectra (Figure 8a) was not observed the band associated to these defects, indicating that we have films with high optical quality without structural defects.

The refractive index (n) and film thickness could be determined from the interference fringes by the envelope method, using the expression reported by Manifacier *et al.*[40] and modified by Peng and Desu,[41] equation 3, where N is defined with equation 4. T_{max} and T_{min} are the transmission maximum and the corresponding minimum at a wavelength λ of the interference fringes (Figure 8a), while n_s is the substrate refractive index silica at the same wavelength.[42] The refractive index values, n, calculated from equations 3 and 4, are shown in Figure 8b for $80SiO_2$:$20GeO_2$ films annealed at 700 °C. The refractive index results have been fitted with the following Sellmeier curve,[43] equation 5.

$$n = [N + (N^2 - n_s^2)^{1/2}]^{1/2} \quad (3)$$

$$N = 0.5(1 + n_s^2) + 2n_s \frac{(T_{max} - T_{min})}{(T_{max}.T_{min})} \quad (4)$$

$$n^2 = A + \frac{B}{\left(\frac{\lambda}{10^3}\right)^2 - C} - D\left(\frac{\lambda}{10^3}\right)^2 \quad (5)$$

The fit of the experimental results with equation 5 provides the following set of parameters: A = 2.2315; B = 0.0040; C = 0.0030; and D = 0.0005 (λ in nm). This Sellmeier curve is shown in Figure 8b. The calculated refractive index presents a good dispersion and it can be well fitted by the Sellmeier relation. The extrapolated values of the Sellmeier curves can be used to calculate the admittance angle and coupling angle when $80SiO_2$:$20GeO_2$ amorphous is used in waveguiding experiments.

Another application of transmission spectra is the film thickness estimation. The thickness d of the layer can be calculated from two adjacent maxima or minima of interference fringes at λ_1 and λ_2 by equation 6,[41] where λ_1, $n(\lambda_1)$ and λ_2, $n(\lambda_2)$ are the corresponding wavelengths and refractive indexes calculated above by the envelope method. The average value of d determined by the equation 6 is 1214 ± 35 nm.

$$d = \frac{(\lambda_1.\lambda_2)}{2[n(\lambda_1).\lambda_2 - n(\lambda_2).\lambda_1]} \quad (6)$$

The refractive index of the bulk glass material is 1.489 at 589.3 nm wavelength.[44] In this work we obtained a refractive index of 1.498, which is similar than that of $80SiO_2$:$20GeO_2$ glass, indicating a high density of our films annealed at 700 °C. This film heat-treated at 700 °C is very important for waveguide design; in the present case, one has a high $\Delta n = 0.040$ at 589.3 nm, $\Delta n = 0.040$ at 632.9 nm, $\Delta n = 0.050$ at 1535 nm wavelengths between the waveguiding layer and the SiO_2 buffer layer (or cladding), such that a guiding layer thickness of 787 nm is already sufficient for single mode propagation (TE_0 or TM_0 mode) at 1535 nm. To excite the second mode (TE1 or TM1), it is necessary to have a film with 2790 nm thickness (these thickness limit values were calculated by relation in the reference 25).

Sigoli *et al.*[21] have obtained a refractive index of ca. 1.453 at 1550 nm for the film thermally treated at 1150 °C with an average thickness of ca. 3.9 mm. The refractive index was lower than that obtained in our work (ca. 1.49) because we used larger amounts of GeO_2 that allow prepare thinner films to have only one guided mode, i.e., thickness of ca. 1.2 mm is enough to guide the first mode (TE_0 or TM_0 mode) in the films of $80SiO_2$:$20GeO_2$ matrix. Probably, films of x = 20 composition having thickness around ca. 2500 nm (6 layers) should be adequate to be applied as waveguides in the NIR region.

An 800 nm Ti-sapphire laser emitting 150 fs, 76 MHz mode-locked pulses was focused on the film surface by an objective lens. The spot size of the focused beam was 5 mm at the focal point, and the average power of the laser was 10 mW. The scanning speed was 0.5 mm s^{-1}. Optical surface image using a microscopy by the reflected visible light and 3D surface profilometry of the channel waveguide measured using a FORMTRACER profilometer from Taylor Hobson Precision model SV-C525 are shown in Figures 9a and 9b. The images illustrated in Figures 9a and 9b show a surface profile and air grooves created by the femtosecond laser etching technique and between two air

grooves there is the waveguide consisting of the Er-doped $80SiO_2$:$20GeO_2$ ribs on silica substrate. The air grooves with a width around 10 mm and a depth of 5 mm, were created by the laser irradiation and the shape and structure of channels are highly reproducible and sharply defined (Figures 9a and 9b). The width and depth of the channels can be tailored changing the position of the spot of the focused beam in order to produce mono or multimodal channel waveguides. In our preliminary experiment we obtained ribs with width of 15 mm.

On the basis of the film thickness and refractive index values, the confinement coefficient of the film

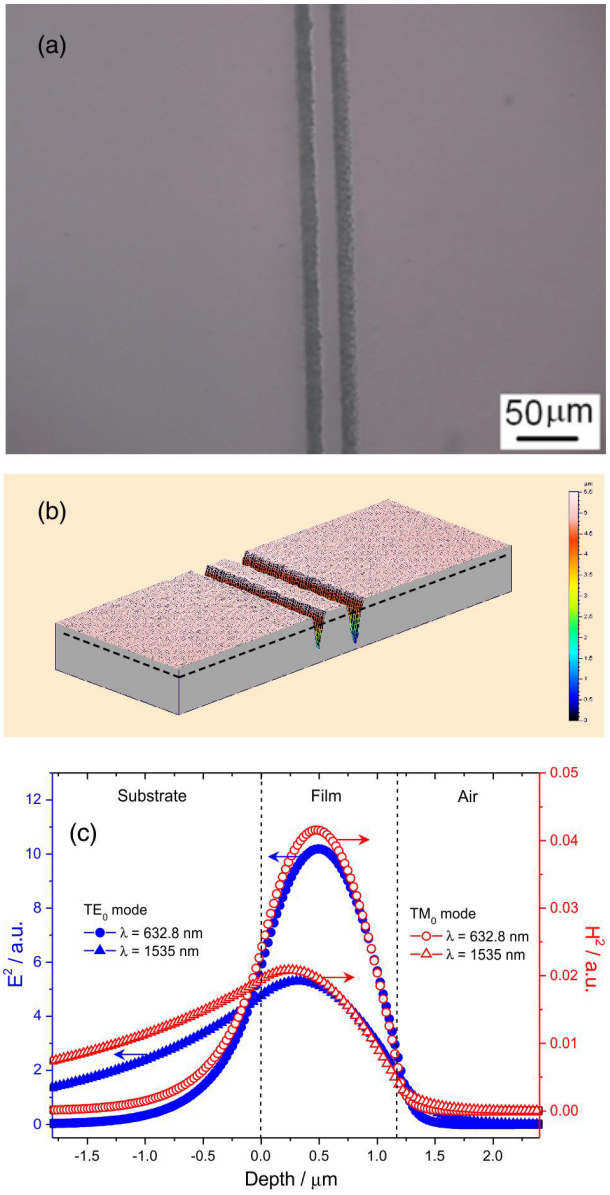

Figure 9. (a) Optical surface image; (b) 3D image of the 15 mm width rib channel waveguide for a film with 1214 nm thickness obtained by femtosecond laser; (c) calculated square electric and magnetic field profiles of the TE_0 and TM_0 modes at 632.8 and 1535 nm along z axis (depth) for the waveguides based on the Er-doped $80SiO_2$:$20SiO_2$.

was estimated. Figure 9c shows the squared electric and magnetic field profiles of the TE_0 and TM_0 modes of the waveguides containing with x = 20 at 632.8 and 1535 nm wavelengths. The values represent the ratio of the integrated intensity, i.e., the square of the electric or magnetic field in the waveguide to the total intensity for each wavelength. The total intensity also includes the squared evanescent fields.[30] A light confinement above 82% can be seen for the waveguides excited at 632.8 nm. For the 1535 nm wavelength, the TE_0 and TM_0 confinement are ca. 50% and ca. 46%. Higher confinement coefficients for TE_0 and TM_0 modes are expected by increasing the film thickness and it is possible to obtain a well confined single mode at 1535 nm, which is the wavelength of interest in integrated optical systems as amplifiers.

The differences between the refractive index of the rib channel waveguide and silica optical fibers are crucial to its application as waveguide amplifiers in telecommunication systems, as well as the rib channel waveguide thickness. The losses by coupling with silica optical fibers increases in compounds with high refractive index and low thickness. In fact, it is necessary to tailor the refractive index and thickness of the rib channel in relation to the commercial optical fibers. But, the refractive index of the rib channel cannot be low, because they are deposited onto silica (same material of the optical fibers), if not the pump and emitted light did not maintain confined. On the other hand, the losses in this sol-gel based planar waveguides are not only due to these parameters. During sol synthesis and film deposition undesirable impurities can be incorporated and/or not be eliminated by heat-treatments, resulting in waveguides with losses of about 1.0 dB cm^{-1}.[28] Although full densification is always achieved together with initial crystallization process, crystalline size need be controlled.[25] Surface roughness should be considered as another source of losses, to reduce these losses the homogeneous and crack-free films should be prepared. Finally, the best composition reported in our work ($80SiO_2$:$20GeO_2$) is close in composition to other systems in the literature, for example, those containing ZrO_2,[28,30] TiO_2,[31] and T_2O_5,[27,29] however present lower refractive index.

Conclusions

In summary, we have used a simple sol-gel route to prepare stable and transparent sols, gels and films. The gels decompositions to form powders were evaluated by TGA and DTA techniques, and endothermal and exothermal events were analyzed. The materials show mass loss from room temperature to around 500 °C. Between 500 and 700 °C, no reactions were observed. The

organic and hydroxyl compounds into the matrix were evaluated by FTIR that reduce gradually by increasing the annealing temperature. At 700 °C, the materials are completely amorphous, but at higher temperatures a silica-rich amorphous phase and GeO_2 nanocrystals with tetragonal structure were obtained. The HRTEM images reveal spherical GeO_2 nanoparticles of around 3.7, 4.6 and 25.0 nm in diameter for x = 10 at 900 °C, x = 10 and x = 20 at 1100 °C, respectively. EDX results show high concentrations of Er^{3+} ions around GeO_2 nanoparticles at 1100 °C. In fact, the GeO_2 nanoparticles formation can allow incorporate higher concentration of active Er^{3+} ions. For x = 10, higher infrared emissions occur in the matrix doped with 0.5 mol% of Er^{3+}, at 900 °C and 1100 °C. But the 1 mol% of Er^{3+} doped $80SiO_2$:$20GeO_2$ compound have an infrared emission around 4.9 times higher than that for 1 mol% Er^{3+} doped $90SiO_2$:$10GeO_2$. The Er^{3+} $^4I_{13/2}$ level has a lifetime between 15.0 ms and 7.5 ms depending on the GeO_2 content and heat-treatment. The optical band gap of 5.79 eV and refractive index values were determined, being ca. 1.498 at wavelength of 589.3 nm, and the Sellmeier parameters were estimated. Films deposited by spin-coating technique present ca. 1214 nm thickness, as calculated by the envelope method. Rib channel waveguides were obtained with width of 15 mm using femtosecond laser radiation, and a light confinement above 82% can be achieved for these waveguides when excited at 632.8 nm.

The chemical procedure using as a precursor TEOS, GeO_2, TMAH is easy, doesn't require special atmosphere, and has relatively low cost. As a final conclusion, the 1mol% of Er^{3+} doped $80SiO_2$:$20GeO_2$ compounds are potentially applicable in integrated optical systems, specially as miniaturized optical amplifiers.

Supplementary Information

Supplementary data (PL spectra) are available free of charge at http://jbcs.sbq.org.br as PDF file.

Acknowledgements

The authors are grateful for the financial support provided by CAPES, CNPq, FAPEG, FAPESP and FUNAPE/UFG Brazilian agencies.

References

1. Henmi, N.; Aoki, Y.; Ogata, T.; Saito, T.; Nakaya, S.; *J. Lightwave Technol.* **1993**, *11*, 1615.
2. Krokhin, O. N.; *Laser Phys.* **2005**, *15*, 1303.
3. Mukhopadhyay, S.; Ramesh, K. P.; Kannan, R.; Ramakrishna, J.; *Phys. Rev. B* **2004**, *70*, 224202.
4. Polynkin, O.; Temyanko, V.; Mansuripur, M.; Peyghambarian, N.; *IEEE Photon. Technol. Lett*. **2004**, *16*, 2024.
5. Cheng, C.; Xiao, M.; *Opt. Commun*. **2005**, *254*, 215.
6. Dejneka, M. J.; Hanson, B. Z.; Crigler, S. G.; Zenteno, L. A.; Minelly, J. D.; Allan, D. C.; Miller, W. J.; Kuksenkov, D.; *J. Am. Ceram. Soc.* **2002**, *85*, 1100.
7. Bulla, D. A. P.; Li, W. T.; Charles, C.; Boswell, R.; Ankiewicz, A.; Love, J. D.; *J. Lightwave Technol*. **2005**, *23*, 1302.
8. Armelao, L.; Gross, S.; Obetti, G.; Tondello, E.; *Surf. Coat. Technol*. **2005**, *190*, 218.
9. Nunzi-Conti, G.; Berneschi, S.; Brenci, M.; Pelli, S.; Sebastiani, S.; Righini, G. C.; Tosello, C.; Chiasera, A.; Ferrari, M.; *Appl. Phys. Lett.* **2006**, *89*, 121102.
10. Pita, R. K.; Yu, S. F.; Tjin, S. C.; Kam, C. H.; *Appl. Phys. Lett.* **2006**, *89*, 071105.
11. Qin, G.; Lu, J.; Bisson, J. F.; Feng, Y.; Ueda, K. I.; Yagi, H.; Yanagitani, T.; *Solid State Commun*. **2004**, *132*, 103.
12. Schubert, U.; Arpac, E.; Glaubitt, W.; Helmerich, A.; Chau, C.; *Chem. Mater*. **1992**, *4*, 291.
13. Liu, J.; Lam, Y. L.; Chan, Y. C.; Zhou, Y.; Que, W. X.; Ooi, B. S.; *Appl. Phys. A* **1999**, *69*, 649.
14. Chang, C. C.; Chen, W. C.; *Chem. Mater*. **2002**, *14*, 4242.
15. Zourob, M.; Mohr, S.; Fielden, P. R.; Goddard, N. J.; *Lab Chip* **2005**, *5*, 772.
16. Jing, C.; Hou, J.; Zhang, Y.; *J. Phys. D: Appl. Phys*. **2006**, *39*, 1174.
17. Shigemura, H.; Kawamoto, Y.; Nishii, J.; Takahashi, M.; *J. Appl. Phys*. **1999**, *85*, 3413.
18. Jang, J. H.; Koo, J.; Bae, B. S.; *J. Non-Cryst. Solids* **1999**, *259*, 144.
19. Yang, H.; Yao, X.; Wang, X.; Gu, X.; Wang, F.; *Opt. Mater*. **2007**, *29*, 631.
20. Que, W.; Wang, L. L.; Chen, T.; Sun, Z.; Hu, X.; *J. Cryst. Growth* **2006**, *288*, 75.
21. Sigoli, F. A.; Messaddeq, Y.; Ribeiro, S. J. L.; *J. Sol-Gel Sci. Technol.* **2008**, *45*, 179.
22. Jing, C.; Hou, J.; Zhang, Y.; *J. Am. Ceram. Soc*. **2007**, *90*, 3646.
23. Siemens A. G.; *Coating Germanium Crystals with a Water Insol Germanium Oxide*, *US pat. 3,525,650-A* **1965** (*CA 842735-A*).
24. Miller, S. E.; *IEEE J. Quantum Electron*. **1972**, *QE-8 part 2*, 199.
25. Lee, D. L.; *Electromagnetism Principles of Integrated Optics*; Wiley: New York, USA, 1986.
26. de Pietro, G. M.; Pereira, C.; Gonçalves, R. R.; Ribeiro, S. J. L.; Freschi, C. D.; Cassanjes, F. C.; Poirier, G.; *J. Am. Ceram. Soc*., *in press*, DOI: 10.1111/jace.13555.
27. Ferrari, J. L.; Lima, K. O.; Maia, L. J. Q.; Ribeiro, S. J. L.; Gonçalves, R. R.; *J. Am. Ceram. Soc*. **2011**, *94*, 1230.

28. Gonçalves, R. R.; Guimarães, J. J.; Ferrari, J. L.; Maia, L. J. Q.; Ribeiro, S. J. L.; *J. Non-Cryst. Solids* **2008**, *354*, 4846.
29. Ferrari, J. L.; Lima, K. O.; Maia, L. J. Q.; Ribeiro, S. J. L.; Gomes, A. S. L.; Gonçalves, R. R.; *J. Nanosci. Nanotechnol*. **2011**, *11*, 2540.
30. Cunha, C. S.; Ferrari, J. L.; Oliveira, D. C.; Maia, L. J. Q.; Gomes, A. S. L.; Ribeiro, S. J. L.; Gonçalves, R. R.; *Mater. Chem. Phys.* **2012**, *136*, 120.
31. Almeida, R. M.; Marques, A. C.; Pelli, S.; Righini, G. C.; Chiasera, A.; Mattarelli, M.; Montagna, M.; Tosello, C.; Gonçalves, R. R.; Portales, H.; Chaussedent, S.; Ferrari, M.; Zampedri, L.; *Philos. Mag.* **2004**, *84*, 1659.
32. Maia, L. J. Q.; Mastelaro, V. R.; Hernandes, A. C.; Fick, J.; Ibanez, A.; *Thin Solid Films* **2009**, *517*, 6584.
33. Melkumov, M. A.; Laptev, A. Y.; Yashkov, M. V.; Vechkanov, N. N.; Guryanov, A. N.; Bufetov, I. A.; *Inorg. Mater.* **2010**, *46*, 299.
34. van den Hoven, G. N.; Polman, A.; Van Dam, C.; Van Uffelen, J. W. M.; Smit, M. K.; *Appl. Phys. Lett*. **1996**, *68*, 1886.
35. Kik, P. G.; Polman, A.; *MRS Bull*. **1998**, *23*, 48.
36. Jha, A.; Richards, B.; Jose, G.; Teddy-Fernandez, T.; Joshi, P.; Jiang, X.; Lousteau, J.; *Prog. Mater. Sci.* **2012**, *57*, 1426.
37. Maia, L. J. Q.; Bernardi, M. I. B.; Feitosa, C. A. C.; Mastelaro, V. R.; Zanatta, A. R.; Hernandes, A. C.; *Thin Solid Films* **2004**, *457*, 246.
38. Nishii, J.; Kitamura, N.; Yamanaka, H.; Hosono, H.; Kawazoe, H.; *Opt. Lett*. **1995**, *20*, 1184.
39. Jang, J. H.; Koo, J.; Bae, B. S.; *J. Am. Ceram. Soc*. **2000**, *83*, 1356.
40. Manifacier, J. C.; Gasiot, J.; Fillard, J. P.; *J. Phys. E: Sci. Instrum*. **1976**, *9*, 1002.
41. Peng, C. H.; Desu, S. B.; *J. Am. Ceram. Soc*. **1994**, *77*, 929.
42. Mazurin, O. V.; Streltsina, M. V.; Shvaiko-Shvaikovskaya, T. P.; *Handbook of Glass Data: Part A-Silica Glass and Binary Silicate Glasses*; Elsevier: New York, USA, 1983.
43. Vázquez, R. M.; Osellame, R.; Marangoni, M.; Ramponi, R.; Diéguez, E.; *Opt. Mater*. **2004**, *26*, 231.
44. Doweidar, H.; *J. Non-Cryst. Solids* **2011**, *357*, 1665.

Submitted: June 15, 2015
Published online: September 1, 2015

FAPESP has sponsored the publication of this article.